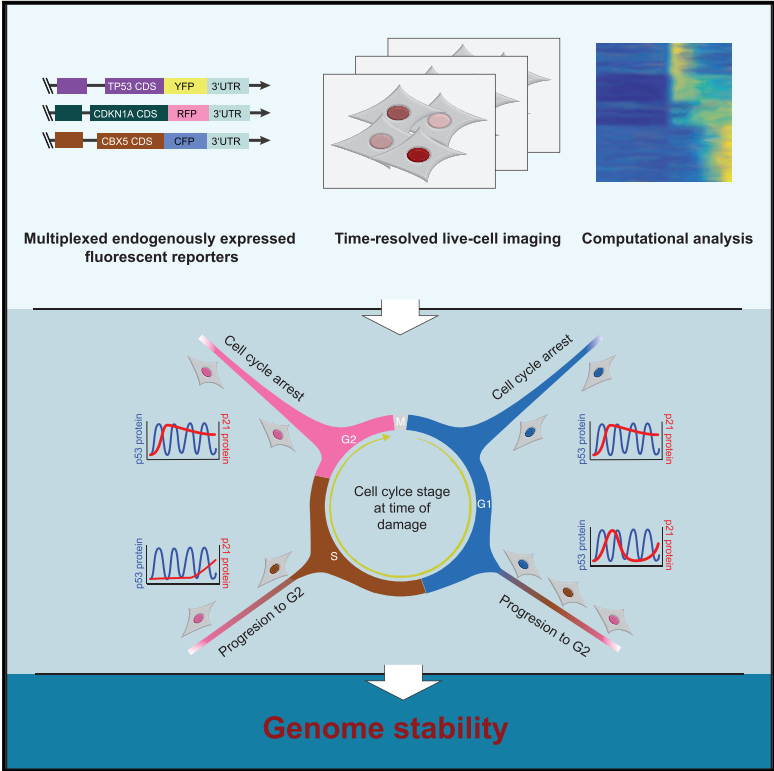


Cell Reports

PCNA-Mediated Degradation of p21 Coordinates the DNA Damage Response and Cell Cycle Regulation in Individual Cells

Graphical Abstract



Authors

Caibin Sheng, Isabella-Hilda Mendler, Sara Rieke, ..., Dhana Friedrich, Barbara Drossel, Alexander Loewer

Correspondence

drossel@fkp.tu-darmstadt.de (B.D.), loewer@bio.tu-darmstadt.de (A.L.)

In Brief

Combining live-cell microscopy of endogenous fluorescent reporters with computational analysis, Sheng et al. investigate how the p53-mediated response to ionizing radiation is adjusted to cellular states. They demonstrate that heterogeneous p21 dynamics post damage are caused by S phase-specific degradation through PCNA-CRL4^{cdt2}, which is necessary for maintaining genome stability.

Highlights

- Single-cell and computational analyses show how signaling adapts to internal states
- The p53 response to damage is posttranscriptionally adjusted to cell cycle states
- PCNA-CRL4^{cdt2}-mediated degradation leads to delayed p21 dynamics during S phase
- Accumulation of non-degradable p21 during S phase induces genome instability



PCNA-Mediated Degradation of p21 Coordinates the DNA Damage Response and Cell Cycle Regulation in Individual Cells

Caibin Sheng,^{1,2} Isabella-Hilda Mendler,³ Sara Rieke,¹ Petra Snyder,¹ Marcel Jentsch,^{1,2} Dhana Friedrich,^{1,2} Barbara Drossel,^{3,*} and Alexander Loewer^{1,2,4,*}

¹Department of Biology, Technische Universität Darmstadt, Darmstadt, Germany

²Berlin Institute for Medical Systems Biology, Max Delbrueck Center for Molecular Medicine, Berlin, Germany

³Physics Department, Technische Universität Darmstadt, Darmstadt, Germany

⁴Lead Contact

*Correspondence: drossel@fkp.tu-darmstadt.de (B.D.), loewer@bio.tu-darmstadt.de (A.L.)

<https://doi.org/10.1016/j.celrep.2019.03.031>

SUMMARY

To enable reliable cell fate decisions, mammalian cells need to adjust their responses to dynamically changing internal states by rewiring the corresponding signaling networks. Here, we combine time-lapse microscopy of endogenous fluorescent reporters with computational analysis to understand at the single-cell level how the p53-mediated DNA damage response is adjusted during cell cycle progression. Shape-based clustering revealed that the dynamics of the CDK inhibitor p21 diverges from the dynamics of its transcription factor p53 during S phase. Using mathematical modeling, we predict and experimentally validate that S phase-specific degradation of p21 by PCNA-CRL4^{cdt2} is sufficient to explain these heterogeneous responses. This highlights how signaling pathways and cell regulatory networks intertwine to adjust the cellular response to the individual needs of a given cell.

INTRODUCTION

Mammalian cells adjust their fate and function to varying requirements during development and adult tissue homeostasis. To enable appropriate decisions, cells integrate incoming signals with information about their internal state and execute corresponding response pathways. Relevant internal states include cell cycle phase, interactions with neighboring cells or the activity level of other signaling pathways (Snijder and Pelkmans, 2011). Consequently, genetically identical cells may react differently to a given stimulus, leading to heterogeneous outcomes during differentiation (Goolam et al., 2016), pathogenesis (Weinberger et al., 2005), or therapy (Cohen et al., 2008; Paek et al., 2016). However, as both signal processing and the regulation of cellular states are dynamic processes, it is not sufficient to determine them at the time of a stimulus, but we need to follow them over time in individual cells.

In this study, we use the DNA damage response (DDR) as a paradigm to understand how individual cells adjust their re-

sponses to dynamically changing internal states. DNA double strand breaks (DSBs) compromise the integrity of the genome and have detrimental consequences if left unrepaired (Ciccia and Elledge, 2010). To counteract these lesions, cells evolved sensitive sensing mechanisms that activate the DDR and induce transient cell cycle arrest in G1 or G2 phase or terminal cell fates, such as senescence and apoptosis (Kastenhuber and Lowe, 2017). A central hub of the DDR is the tumor suppressor p53. This transcription factor is activated by damage-responsive kinases and controls the cellular response by inducing the expression of its target genes (Riley et al., 2008). p53 itself is regulated by feedback loops: in the absence of DNA damage, it is ubiquitinated by the E3 ligase Mdm2 and degraded by the proteasome (Haupt et al., 1997). Upon damage, posttranslational modifications of p53 and Mdm2 prevent their interaction and allow p53 to accumulate in the nucleus where it binds to target gene promoters and induces their expression. Among them are negative regulators, such as Mdm2 and the phosphatase Wip1, which terminate the response. If damage persists, p53 accumulates repeatedly in pulses of uniform amplitude and duration (Batchelor et al., 2009; Loewer et al., 2010; Purvis et al., 2012).

A prominent p53 target gene is the cyclin-dependent kinase (CDK) inhibitor p21. It is crucial for arresting the cell cycle at the G1-S transition upon DNA damage through inhibition of CDK2/4 (Deng et al., 1995) and may contribute to the arrest in G2 phase by inhibiting CDK1 (Bunz, 1998). Moreover, p21 is essential for preventing endoreduplication during extended cell cycle arrest (Toettcher et al., 2009) and for induction of cellular senescence (Muñoz-Espín and Serrano, 2014). In addition to its function as a CDK inhibitor, p21 also contributes to regulating DNA replication by binding the proliferating cell nuclear antigen (PCNA) and modulating its interaction with alternative DNA polymerases involved in *trans*-lesion synthesis (Mansilla et al., 2013).

In the present study, we aimed to understand how the dynamic p53-driven response to DNA damage is adjusted dynamically to the internal state of individual cells. To this end, we generated a live-cell reporter expressing fusion proteins of p53 and p21 with fluorescent proteins from endogenous gene loci. Combining time-lapse microscopy, noninvasive cell cycle profiling, and shape-based clustering, we identified heterogeneous p21 responses that were uncoupled from p53 dynamics. We show that the observed heterogeneity in p21 levels is



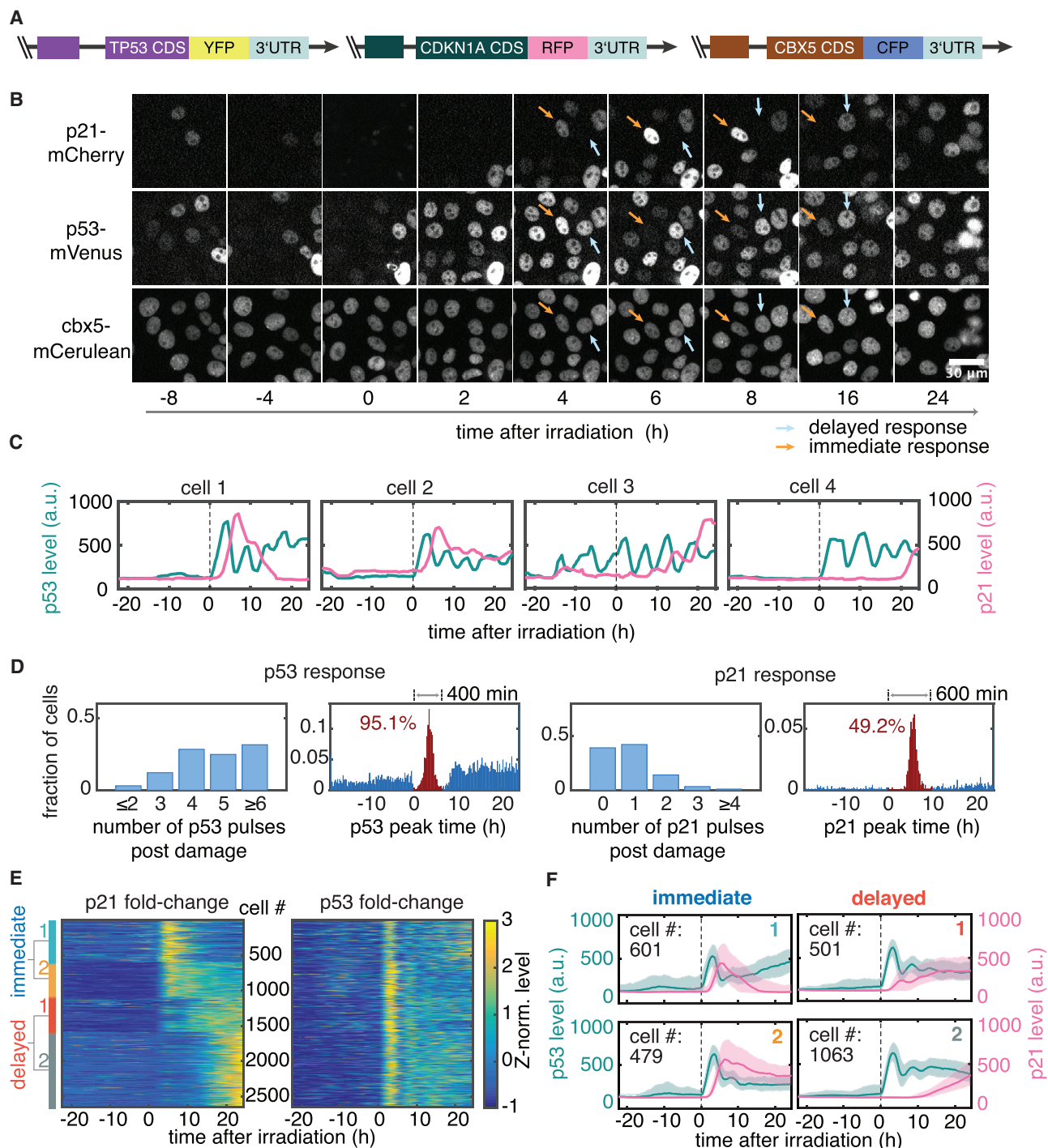


Figure 1. Dynamics of p53/p21 Proteins Are Diverse after DNA Damage in Single Cells

(A) Endogenous reporter system to simultaneously measure p53/p21 in the same cells. Sequences coding for fluorescent proteins were inserted between the coding sequences (CDSs) and 3' untranslated regions (3'UTRs) using CRISPR/Cas9-mediated genome editing (see also Figure S1).

(B) Live-cell time-lapse microscopy images of MCF10A cells expressing p21-mCherry/p53-mVenus at selected time points. Cells were imaged for 24 h, irradiated with 5Gy ionizing radiation, and followed for additional 24 h. Two example cells with different responses are indicated with colored arrows (see also Video S1). Scale bar, 30 μ m.

(C) Four example time series demonstrating diverse p53 (green) and p21 (magenta) dynamics in individual cells. Dashed lines indicate the time of irradiation.

(D) Quantification of the number and timing of p53 and p21 pulses over the experimental period shows heterogeneous responses in cell populations. See also Figures S2C–S2F for feature definition and dose-dependent analysis. Pulses occurring within 400 min (p53) and 600 min (p21) after irradiation are highlighted in

(legend continued on next page)

determined by the initial cell cycle state at the time of damage and its progression during the damage response. Through mathematical modeling and genome engineering, we show that the underlying molecular mechanism depends on the interaction of PCNA and p21 during S phase and subsequent CRL4^{cdt2}-mediated proteasomal degradation. Our results highlight how signaling pathways and cell regulatory networks intertwine to adjust the cellular response to the individual needs of a given cell.

RESULTS

p21 Dynamics after DNA Damage Diverge from p53 Dynamics in Single Cells

To monitor endogenous p53 and p21 protein levels in individual cells over time, we applied Cas9-mediated genome engineering in the nontransformed diploid breast-epithelial cell line MCF10A to generate C-terminal fluorescent protein fusions (Figures 1A and S1A). In addition, we tagged endogenous Cbx5 as nuclear marker to facilitate automated cell tracking (Cohen-Saidon et al., 2009; Strasen et al., 2018). Using p53 as a paradigm, we validated that heterozygous insertions are sufficient for monitoring the dynamics of endogenous proteins, as expression from differentially tagged alleles was highly correlated (Figure S1B). Accordingly, we observed high correlation between the levels of p53-mVenus and total p53 in individual cells with heterozygous insertions (Figures S1C and S1D). We further validated that fusion of mVenus to endogenous p53 did not alter protein dynamics and cell cycle arrest upon irradiation (Figures S1E, S1F, and S1H–S1I). When we engineered both p53 and p21 in the same cell line, the p53 response was unaltered as well, and we only observed a slight stabilization of p21 and minor changes in cell cycle arrest upon damage induction (Figures S1G and S1J).

Using live-cell microscopy, we monitored protein levels for ~20 h during proliferation before challenging cells with 5Gy ionizing radiation and followed them for additional 24 h (Figure 1B). Before irradiation, we observed asynchronous pulses of p53 accumulation as previously described (Loewer et al., 2010). Infrequently, these pulses correlated with transient p21 induction. Upon damage induction, p53 accumulated in almost all cells and reached peak levels at about 4 h. The initial p53 response was followed by regular pulses of protein accumulation (Figures 1B and 1C; Video S1). In contrast, we observed heterogeneous p21 responses post irradiation: in some cells, p21 accumulated right after p53 induction, while others showed a delay of several hours before upregulating p21 protein levels (Figures 1B and 1C).

To systematically analyze p53 and p21 responses, we extracted number and timing of accumulation pulses for thousands of cells. In over 95% of cells, we observed p53 pulses within 400 min after irradiation, while a corresponding peak of p21

accumulation was present in only half of the cells (Figure 1D). Moreover, most cells showed only one p21 pulse despite repeated p53 pulses (Figures 1D and S2F). Similar homogeneous p53 and heterogeneous p21 responses were observed upon higher irradiation doses, excluding that varying damage levels caused diverging p21 dynamics (Figures S2A–S2F).

Heterogeneity in p21 Dynamics Is Determined by Cell Cycle State and Progression

To gain deeper insights into heterogeneous p21 responses, we grouped time-series data according to shape-based distance (SBD) (Paparrizos and Gravano, 2015). SBD tolerates both amplitude and time variances, allowing pairwise comparisons of single-cell trajectories. Combining binary tree and k-centroid clustering, we grouped cells into four subgroups (Figures 1E, 1F, and S2G). In this analysis, about 40% of cells reacted with immediate accumulation of p21 post damage. These cells could be further stratified into subgroups with different duration of p21 accumulation (Figure 1F). The remaining cells showed delayed p21 responses and were further classified into subgroups according to the timing of p21 accumulation (Figure 1F).

We next determined for each cell the cell cycle phase at time of damage and at the end of the observation period. Cell cycle stages at damage induction were estimated from the timing of the last division before irradiation, which was identified as bisection of nuclear marker intensity (Figures 2A and S3A). We confirmed this approach in an independent experiment using 5-ethynyl-2'-deoxyuridine (EdU) labeling and staining of cell cycle markers (Figure 2B). To determine cell cycle states at the end point, cells were labeled with EdU during the last 30 min of the experiment, and nuclear sizes as well as DNA contents were measured using an intercalating dye. Based on these measurements, we constructed a semisupervised classification process (Figures 2A, 2C, and S3B–S3F) and validated it by comparison to flow cytometry data (Figure S3G).

This classification indicated that cells showing an immediate p21 response were mainly damaged in G1 or G2 phase (Figures 2D, S4A, and S4B), which was validated by 5-bromo-2'-deoxyuridine (BrdU) staining (Figure S4E). Most of these cells remained arrested in the initial cell cycle phase and showed sustained accumulation of p21. Another part of cells damaged in G1 phase progressed through the cell cycle and ended in either S or G2 phase. Interestingly, these cells showed only transient p21 responses (Figures 2D, S4A, and S4B). In cells progressing all the way to G2 phase, we again observed increasing p21 levels at the end point.

Based on our cell cycle estimation, most cells showing a delayed p21 response were damaged during S phase and arrested in G2 phase (Figures 2D, S4C, and S4D). They were mainly distinguished by the onset of p21 accumulation, which correlated with the time of the last division before damage induction

red and the integrated fraction of cells is indicated. p53 pulses with negative peak time correspond to p53 pulses during normal cell cycle progression. See main text and STAR Methods for further detail (n = 2644 cells).

(E) Cells were stratified into four subgroups of different responses by stepwise binary shape-based clustering (see STAR Methods). Each line represents a single cell with color indicating Z-normalized fold-change. Cell numbers are indicated in Figure 1F.

(F) Population level of subgroups. Lines indicate the median protein levels in each group over time, shaded areas indicate the 25th to 75th percentile (green, p53; magenta, p21). The number of cells in each subgroup is indicated. Results are representative for five independent replicates.

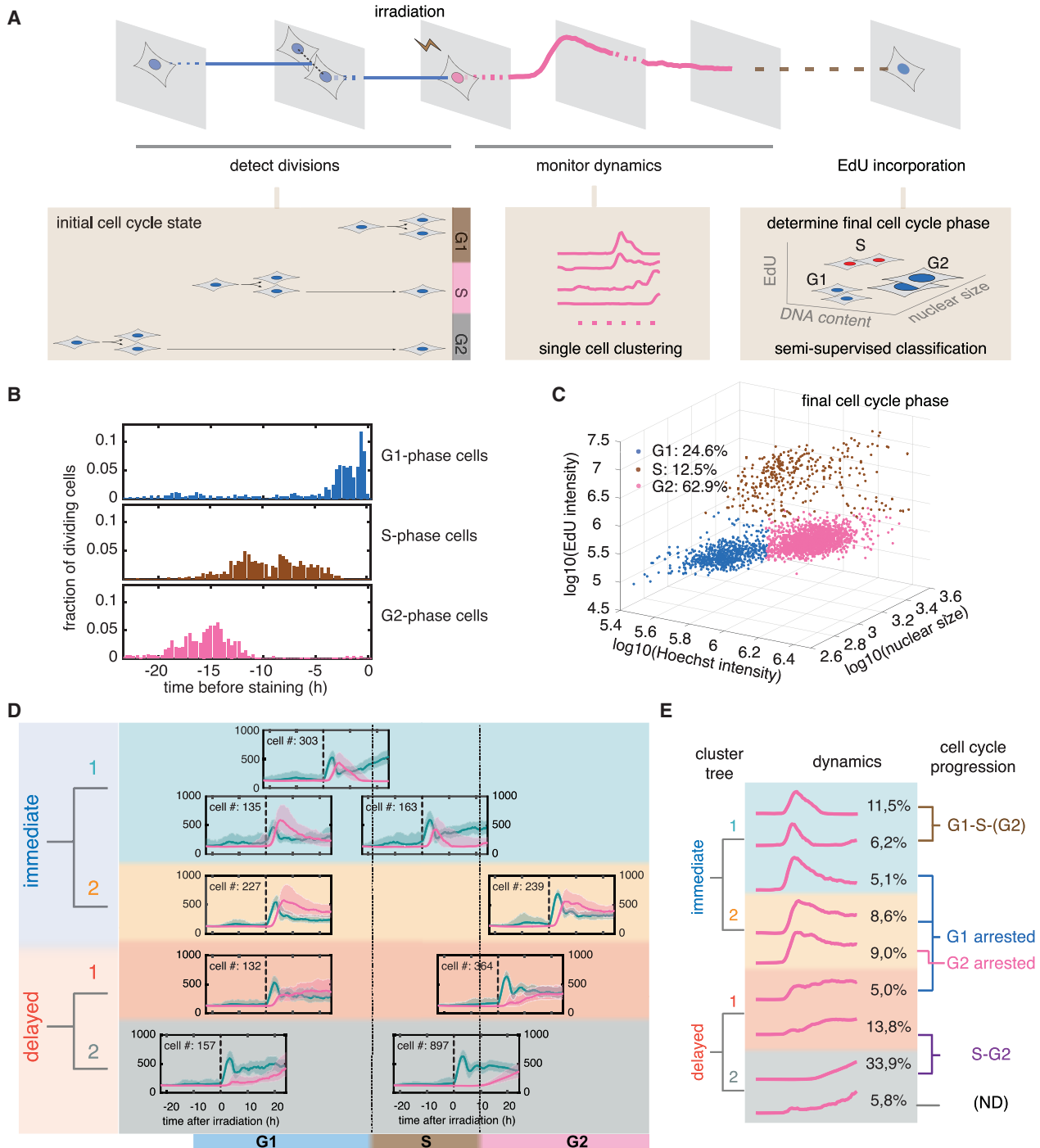


Figure 2. p21 Dynamics Depend on Cell Cycle State and Progression

(A) Experimental integration of cellular dynamics and cell cycle progression. We estimated the initial cell cycle state by monitoring time of division before damage induction. We then analyzed cell cycle states at experimental endpoints by measuring EdU incorporation as well as nuclear size and DNA content by Hoechst staining. Finally, we combined cell cycle measurements with clustered single cell time series of p53 and p21 protein levels (see also Figure S3).

(B) Correlation between the time of division and cell cycle state under normal condition was confirmed by EdU labeling and immunofluorescence staining of cell cycle markers. $p21^{R/+}/p53^{Y/+}/cbx5^{C/C}$ cells were imaged for 24 h and cell division events were recorded. EdU was added in the medium to label S phase cells 30 min before the end. Right after imaging, single cell immunofluorescence staining was performed to determine G1 phase (CyclinB1^{low}) cells and G2 phase (CyclinB1^{high}) cells ($n = 737, 923, \text{ and } 644$ for G1, S, and G2 phase cells).

(legend continued on next page)

(Figures S4F and S4G). Our observation of reduced p21 levels during S phase was consistent with previous reports in S phase arrested or synchronized cells (Ciznadija et al., 2011; Gottifredi et al., 2001, 2004) and could be validated in additional epithelial cell lines (Figure S4H). Synchronization in G2 provided evidence for a causative relationship between delayed p21 accumulation and cell cycle state (Figure S4I).

Based on time of last division, we noticed that about 10% of cells classified as having a “delayed” p21 response were damaged in G1 phase. Re-examining their p21 response revealed that these cells showed an immediate and sustained response, albeit at lower amplitude, and remained arrested in G1 (“delayed 1,” Figures 2D and S4C. For about 160 cells, the initial cell cycle phases could not be identified unambiguously, as division times before damage were evenly distributed. Most of these cells divided after damage. Their p21 response was characterized by a low immediate response followed by increasing p21 levels at later time points. Taken together, we observed that p21 dynamics upon irradiation depend on the initial cell cycle phase and cell cycle progression during the damage response (Figure 2E).

Cell Cycle-Specific p21 Degradation Is Sufficient to Explain Heterogeneous Responses upon Irradiation

Previous studies showed that p21 degradation is tightly regulated during cell cycle progression (reviewed in Starostina and Kipreos, 2012). To test whether cell cycle specific p21 degradation would be sufficient to explain the observed heterogeneity in individual irradiated cells, we established a corresponding delay differential equation model (Figure 3A; Table 1; STAR Methods):

$$\frac{d[p21(t)]}{dt} = \begin{cases} \frac{m \cdot [p53(t - \tau)]^n}{\theta^n + [p53(t - \tau)]^n} - \delta \cdot [p21(t)], & \text{cell in G1 or G2} \\ \frac{m \cdot [p53(t - \tau)]^n}{\theta^n + [p53(t - \tau)]^n} - \delta \cdot D_S \cdot [p21(t)], & \text{cell in S} \end{cases}$$

In this model, p21 production is represented by a Hill function with maximum production rate m , Hill coefficient $n = 4$ due to tetramerization of p53 and activation threshold θ . The time delay $\tau = 1.4$ h reflects the duration of transcription and translation. Degradation of p21 is reflected by a first-order process, which is increased between 25- and 100-fold during S phase (factor D_S). Background-subtracted p53 trajectories were taken as input to fit the model to measured p21 data of thousands of cells. For individual fits, we observed that our abstract model was sufficient to reproduce p21 levels in G1 and G2 arrested

cells (Figures 3B and 3C). However, we observed a systematic deviation of the timing and amplitude of the p21 peak in the median of all fits (Figures 3B, 3C, and S5A). We therefore separately fitted p21 dynamics for only the first 10 h after irradiation. This led to a better reproduction of peak p21 levels but to larger deviations at later times (Figures S5B and S5C), indicating that cells react differently to the first and to later p53 pulses (Chen et al., 2016). When we examined fits for cells in S phase, we found that our model was able to reproduce p21 dynamics (Figures 3D and 3E). In particular, the delayed accumulation of p21 for cells damaged in S phase was well reflected. Similarly, prompt pulse-like p21 responses were observed for cells transitioning from G1 to S phase post damage, regardless of the precise value of D_S (Figure S5D). Distributions of the other fitted parameters were overlapping for all cell cycle profiles (Figure S5E).

An alternative explanation for low p21 levels during S phase is a decrease in p53-mediated p21 production (Beckerman et al., 2009; Gottifredi et al., 2001; Mattia et al., 2007). Surprisingly, the corresponding model fitted single cell data and population averages equally well (Figures S5F–S5H; STAR Methods). We only noted that the initial model better reproduced the steep decrease of p21 frequently happening at the G1/S transition (Figure S5I). We could further improve its fit by implementing a biologically plausible gradually increasing p21 degradation (Figures S5J–S5L), while there was conceptually no further possibility to increase the steepness of the p21 decrease in the alternative model.

As our modeling efforts could not distinguish unambiguously between the two possible explanations for heterogeneous p21 responses in S phase cells, we tested both experimentally. To investigate p21 production, we inserted a destabilized red fluorescent protein preceded by a porcine teschovirus-1 self-cleaving 2A peptide (P2A) sequence at its endogenous locus (Figure 3F). As the P2A sequence leads to separation of both polypeptides during translation, the red fluorescent protein (RFP) signal serves as a reporter for p21 production. Using this reporter, we observed similar RFP accumulation in S and G1/G2 phase cells post damage, arguing against cell cycle specific p21 production rates (Figure 3G). We validated this result using single-molecule fluorescent *in situ* hybridization (Figure 3H).

Multiple cell cycle dependent degradation mechanisms exist for p21 (Figure S6A) (Ng et al., 2003; Starostina and Kipreos, 2012) with PCNA/CRL4^{cdt2}-mediated degradation responsible for low p21 levels during S phase (Figure 3I) (Havens and Walter, 2009). To test whether this mechanism is sufficient to explain the observed heterogeneity in individual irradiated cells, we prevented the interaction between PCNA and p21 by mutating its PCNA-interacting peptide box (PIP box, Galanos et al., 2016)

(C) Final cell cycle phases at 24 h post damage were determined by EdU labeling and measurements of nuclear size and content. S phase cells were determined by an edge detection algorithm (see also Figure S3B). As neither DNA content or nuclear size was sufficient to individually separate G1 and G2 phase cells (see also Figures S3C and S3D), we built a two parameter-based unsupervised classification to identify G1 and G2 phase cells.

(D) Identified subgroups of p53/p21 responses were further stratified according to initial cell cycle state and cell cycle progression. For each graph, the placement indicates cell cycle properties for the corresponding subgroup, with the left side of the plot indicating the initial cell cycle state at the time of damage induction and the right side the final cell cycle state. If a plot is restricted to a single cell cycle phase, the corresponding cells arrested after damage. A plot covering multiple phases indicates cell cycle progression during the damage response. Please note that cell cycle phases are not drawn to scale. Lines indicate the median protein levels in each group over time, shaded areas indicate the 25th to 75th percentile (green, p53; magenta, p21). The number of cells in each group is indicated. See also Figure S4 for detailed analysis.

(E) Correlation between p21 dynamics and cell cycle progression. The percentage of cells in each subgroup is indicated.

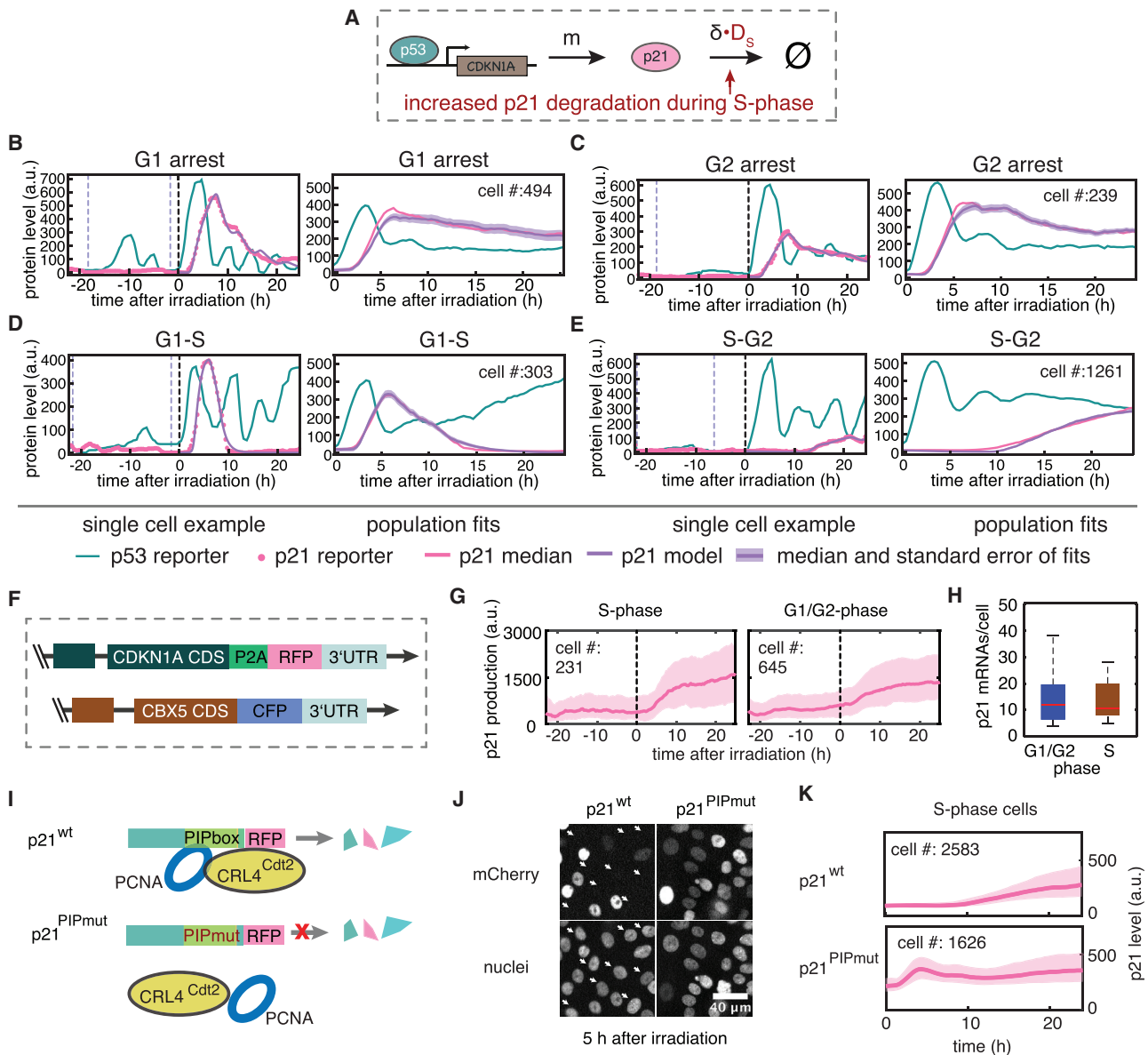


Figure 3. S Phase-Specific Degradation Determines Heterogeneity of p21 Response

(A) Schematic representation of the implemented model with increased p21 degradation during S phase. (B–E) Comparison of simulated (purple) and measured (magenta) p21 protein levels. Protein dynamics in single cells (left) and medians for multiple cells with the same cell cycle characteristics (right) are shown. The number of cells analyzed in each category is indicated. Black dashed lines indicate the time of irradiation (5Gy), blue dashed lines cell divisions. Shaded regions represent the standard error of the median. (F) Endogenous reporter system to measure p21 production rate. A self-cleaving peptide was inserted between coding sequences of p21 and mCherry. (G) p21 production rate remains high during S phase. Transcriptional reporter was imaged for 24 h, incubated in EdU-containing medium for 30 min and subjected to 5Gy irradiation, followed by another 24-h imaging and EdU detection. EdU signals were used to isolate S- and G1/G2 phase cells. Basal signals of mCherry reflecting basal transcription of p21 were subtracted. The resulting levels indicate p21 production rate induced by irradiation. Cell numbers are indicated. (H) smFISH measurements indicate similar RNA levels of S- and G1/G2 phase cells 4 h after irradiation. Cell cycle-specific RNA levels were determined by smFISH and EdU labeling in wild-type MCF10A cells (see STAR Methods). (I) Schematic illustration of PCNA-mediated degradation of p21 and an engineered model to interfere with this degradation (see also Figures S6B and S6C). (J) p21^{PIPmut} accumulated during all cell cycle phases upon damage. p21^{PIPmut} and control cells (p21^{wt}) were irradiated with 5Gy ionizing radiation and examined after 5 h. Arrows indicate p21^{wt} cells with delayed responses. Scale bar, 40 μ m. (K) p21^{PIPmut} accumulated during S phase upon damage induction. S phase p21^{PIPmut} cells and control cells (p21^{wt}) cells were pulse-labeled with EdU, subjected to 5Gy ionizing radiation and imaged for 24 h. Lines indicate the median protein levels of EdU-positive cells in each group over time, shaded areas the 25th to 75th percentile. Cell numbers are indicated. See also Figure S5.

Table 1. Constraints and Start Values for Estimation of Model Parameters

Parameter	Unit	Constraints for Fit	Interval from which Start Values for Fits Were Randomly Chosen
m	$[m] = C_{a.u.} h^{-1}$	$0 < m < 100$ Max(p21 data)	[100, 2000]
θ	$[\theta] = C_{a.u.}$	$0 < \theta < \text{Max}(p53 \text{ data})$	$[0.25 \cdot \text{Max}(p53 \text{ data}), \text{Max}(p53 \text{ data})]$
δ	$[\delta] = h^{-1}$	$0 < \delta < 1.0$	[0, 1.0]
t_S	$[t_S] = h$	$23 < t_S < 46$	[23, 46]

$C_{a.u.}$ are arbitrary concentration units and t_S indicates the beginning (for cells irradiated in G1 and progressing to S phase) or the end of S phase (for cells irradiated in S phase and progressing to G2). Time t_S is counted from the beginning of the experiment.

through genome engineering. As degradation of p21 during S phase may be necessary for proliferation, we added a small molecule-assisted shutoff (SMASH) tag, which degrades p21^{PIPmut} in presence of asunaprevir (ASV) to permit proliferation (Figures S6B–S6E) (Chung et al., 2015). Before experiments, we removed ASV to allow p21^{PIPmut} to freely accumulate. Interestingly, p21^{PIPmut} showed a homogeneous response after damage induction and accumulated immediately in S phase cells (Figures 3J and 3K; Video S2).

PCNA-Mediated Degradation Determines Heterogeneous p21 Dynamics and Protects Genomic Integrity upon DNA Damage

To determine how altered PCNA-p21 interactions influence the damage response, we performed a double-pulse labeling experiment with BrdU and EdU and grouped mutant cells according to cell cycle progression (Figures 4A, 4B, S6F, and S6G). As expected, dynamics of mutant and wild-type p21 were similar in G1 and G2 arrested cells (compare Figure 4B with Figure 2D). In S phase, p21^{PIPmut} accumulated immediately as described above. Surprisingly, levels of mutated p21 peaked around 4 h and subsequently decreased in most cell cycle phases. To investigate if this was a consequence of pulsatile p53 dynamics or indication of p21 degradation by alternative mechanisms, we fitted our abstract mathematical model to the corresponding single cell data. We were able to fit p21 dynamics from both G1/G2-arrested cells and cells progressing through S phase with the same equation and overlapping parameter distributions, including only p53-mediated p21 production as well as unregulated first-order degradation; therefore, we conclude that upon irradiation, the contribution of other p21 degradation mechanisms is neglectable in MCF10A cells (Figures 4C and S6H).

Next, we investigated how accumulation of mutated p21 during S phase affected cell cycle progression and observed a noticeable increase in the number of cells in G1 phase. This emphasizes the contribution of Ctd2-mediated degradation to rapid removal of p21 around the G1-S transition (Barr et al., 2017) and indicates a stronger G1 checkpoint in absence of p21-PCNA interactions (Figures 4D and S6I). In contrast, the fraction of cells in S phase was marginally lower in mutant compared with wild-type cells, providing no sign for severely delayed S phase progression. Furthermore, we found no indication of increased endoreduplication, which was suggested in previous studies (Kim et al., 2008).

Despite a relatively minor effect on cell cycle progression, we observed an increased frequency of chromosomal aberration

24 h after damage induction, most notably chromosome fusions (Figures 4E and 4F). These aberrations led to increased formation of micronuclei after cells completed mitosis (Figure 4G). Together, these results indicate that accumulation of mutant p21 during S phase led to either decreased repair efficiency or additional damage due to malfunctioning replication. This increase in genomic instability led to an increased induction of terminal cell fates, specifically senescence (Figure 4H).

DISCUSSION

To mediate reliable cell fate decisions, cellular signaling needs to efficiently process information in a noisy environment and integrate it with dynamically changing internal states. Previous studies showed that excitability in the p53 network allows to sense DNA damage with high specificity, sensitivity, and robustness by inducing uniform accumulation pulses of the tumor suppressor (Batchelor et al., 2008; Mönke et al., 2017). A filter based on posttranslational modifications subsequently differentiates between transient damage during normal proliferation and sustained damage upon external insults by keeping accumulating p53 inactive and preventing expression of target genes, such as p21 (Loewer et al., 2010). In this study, we highlight another layer of regulation where the p53 response is shaped according to the internal state of the cell. Despite relatively homogeneous p53 dynamics upon ionizing radiation, p21 responses were highly diverse, as has been previously reported for synchronized cell populations (Ciznadija et al., 2011) or in cancerous MCF7 cells (Stewart-Ornstein and Lahav, 2016). Using a combined computational and experimental approach to link signaling dynamics to cell cycle state and cell fate determination in thousands of unperturbed living cells, we show that S phase-specific PCNA/CRL4^{cdt2}-mediated p21 degradation is sufficient to fully explain the observed heterogeneity.

Cells need p21 degradation for faithful repair and replication of the genome, as inappropriate p21 accumulation during S phase led to increased genomic instability. Due to modulating the binding of DNA polymerase- δ and ϵ as well as DNA methyltransferase-1 (DNMT1) to PCNA, high p21 levels may interfere directly with replication (Abbas and Dutta, 2009; Cazzalini et al., 2010). In addition, it was shown that exogenous overexpression of p21 can lead to deregulated origin licensing and replication stress (Galanos et al., 2016). Alternatively, p21 accumulation may interfere with homology dependent repair, which relies on CDK activity at multiple stages (Esashi et al., 2005; Huertas et al., 2008; Ira et al., 2004).

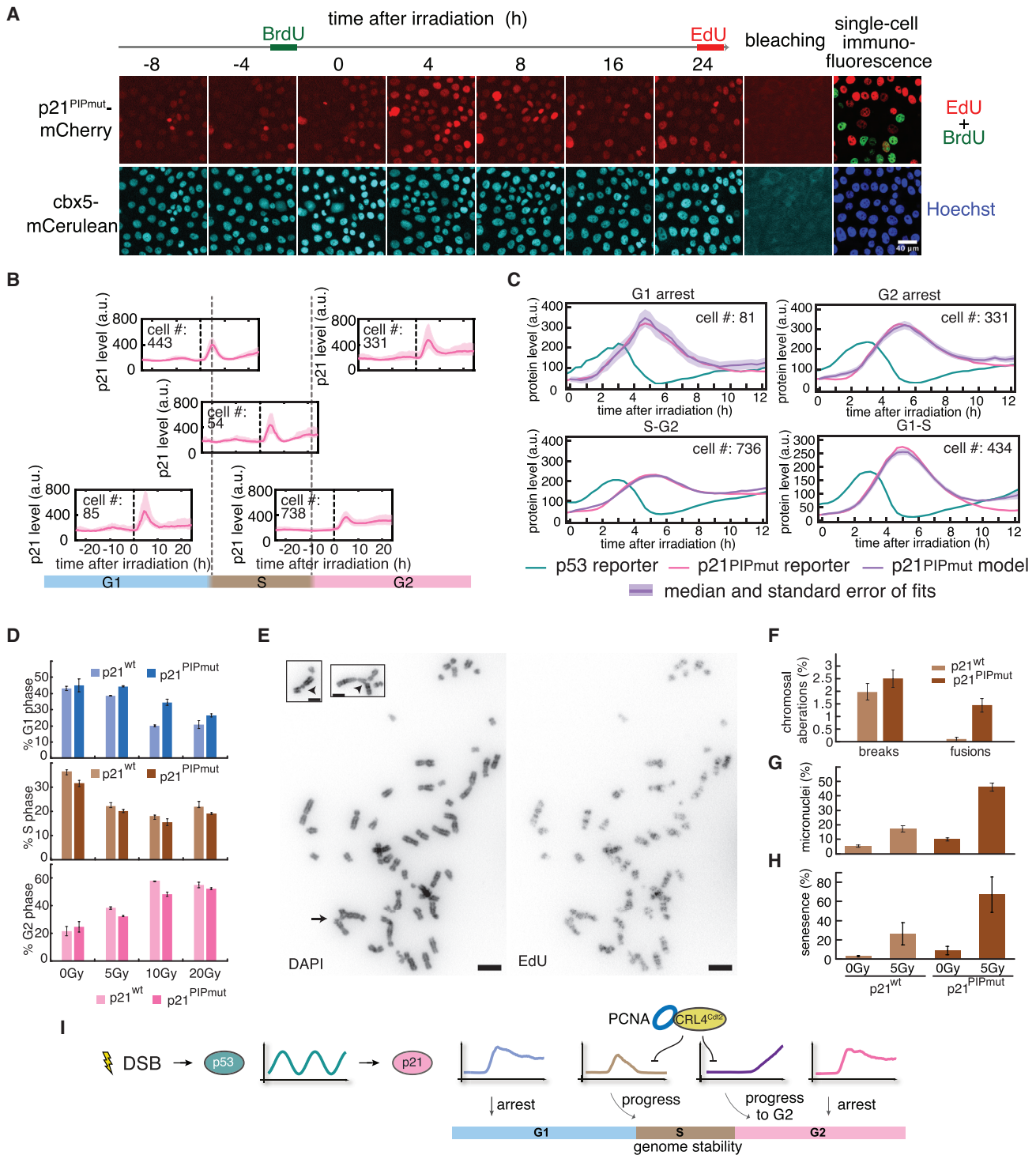


Figure 4. PCNA-Mediated Degradation Determines Heterogeneous p21 Response

(A) Double-pulse labeling experiment was performed to determine cell cycle progression in p21^{PIPmut} cells. p21^{PIPmut} cells were imaged for 24 h in the absence of ASV, incubated in BrdU-containing medium for 30 min, subjected to 5Gy ionizing radiation and imaged for another 24 h, followed by EdU incorporation for 30 min, fluorescence bleaching, and single-cell immunofluorescence to detect BrdU and EdU signals (see also Video S2). Scale bar, 40 μ m.

(B) p21^{PIPmut} shows homogeneous dynamics. Cell cycle progression was determined by combining cell division analysis and quantification of BrdU and EdU signals. The dynamics of p21^{PIPmut} are independent of cell cycle state and cell cycle progression. See Figure 2D for detailed explanations. Cell numbers are indicated.

(legend continued on next page)

Interestingly, we observed a bifurcation in the response of cells damaged in G1, as they either arrested or progressed to S phase. This bifurcation was reflected in the corresponding p21 dynamics, while the p53 response remained relatively homogeneous. Our analysis of kinetic patterns suggests that again degradation rates might differ (Figure S4J). Recent research showed that the ubiquitin ligases CRL4^{Cdt2} and SCF^{Skp2} together mediate p21 degradation before the G1-S transition in undamaged cells (Barr et al., 2017). The increased fraction of G1 cells observed in p21^{PIPmut} cells indicates that upon damage induction, CRL4^{Cdt2}-mediated degradation contributes to restricting the G1 checkpoint as well. In contrast, we did not observe indications that alternative mechanisms such as SCF^{Skp2}- or Mdm2-mediated degradation during late G1 and early S phase (Jin et al., 2003, 2008) contribute noticeably to shaping p21 dynamics upon DNA damage.

Integrating information about the cellular state at the level of target gene stability allows the p53 network to fine-tune its response while maintaining robust activation of its many response genes. It will now be interesting to systematically characterize how other target genes such as pro- or antiapoptotic proteins are regulated during cell cycle progression and the DNA damage response. Understanding heterogeneous p53 responses will be important in the context of cancer therapy as well, as they correlate with drug resistance (Paek et al., 2016).

STAR★METHODS

Detailed methods are provided in the online version of this paper and include the following:

- KEY RESOURCES TABLE
- CONTACT FOR REAGENTS AND RESOURCE SHARING
- EXPERIMENTAL MODEL AND SUBJECT DETAILS
 - Cell lines
- METHOD DETAILS
 - Plasmids and cloning
 - Cell line engineering
 - Time-lapse microscopy
 - Image analysis
 - Single cell clustering
 - Feature analysis of single cell trajectories
 - Cell cycle progression

- Flow cytometry-based cell cycle analysis
- Single-cell Immunofluorescence
- smFISH hybridization
- Immunoblotting
- Metaphase chromosome analysis
- Senescence-associated β -Galactosidase assay
- Mathematical modeling
- QUANTIFICATION AND STATISTICAL ANALYSIS
- DATA AND SOFTWARE AVAILABILITY

SUPPLEMENTAL INFORMATION

Supplemental Information can be found online at <https://doi.org/10.1016/j.celrep.2019.03.031>.

ACKNOWLEDGMENTS

We thank Andrea Grybowski and Silke Dusatko for technical support, Stefan Bohn for important material, and Qingyao Huang, Michael Ensminger and Patrik Weber for helpful discussion. This work was supported by grants and fellowships from China Scholarship Council (to C.S.), German Research Foundation (GRK1657 to I.M. and C.S.), and Einstein Foundation and German Cancer Aid (project number 111645 to A.L.).

AUTHOR CONTRIBUTIONS

C.S., S.R., and P.S. performed experiments and C.S. analyzed data. I.M. constructed DDE modeling. D.F. performed smFISH, and M.J. contributed to image processing. C.S., I.M., B.D., and A.L. wrote the manuscript with contributions from all authors. B.D. and A.L. supervised this work.

DECLARATION OF INTERESTS

The authors declare no competing interests.

Received: July 11, 2018
Revised: January 3, 2019
Accepted: March 8, 2019
Published: April 2, 2019

REFERENCES

- Abbas, T., and Dutta, A. (2009). p21 in cancer: intricate networks and multiple activities. *Nat. Rev. Cancer* 9, 400–414.
- Barr, A.R., Cooper, S., Heldt, F.S., Butera, F., Stoy, H., Mansfeld, J., Novák, B., and Bakal, C. (2017). DNA damage during S-phase mediates the proliferation-quiescence decision in the subsequent G1 via p21 expression. *Nat. Commun.* 8, 14728.

(C) Comparison of simulated (purple) and measured (magenta) median p21^{PIPmut} protein levels for multiple cells with the same cell cycle characteristics. The number of cells analyzed in each category is indicated. Shaded regions represent the standard error of the median.

(D) Cell cycle distributions were measured by flow cytometry 24 h after treatment with the indicated doses of ionizing radiation in wild-type and p21^{PIPmut} cells. Error bars indicate standard deviation of triplicates. Results are representative for three independent experiments.

(E) Accumulation of mutant p21 during S phase increased genome instability. p21^{PIPmut} cells irradiated (5Gy) during S phase (positive EdU staining) showed chromosomal aberrations in metaphase spreads, including chromosome fusions (arrow, large image) and breaks (arrow heads, insets). Scale bars represent 10 μ m (large image) or 5 μ m (insets).

(F) Quantification of chromosomal aberrations 24 h after irradiation (5Gy) in wild-type and p21^{PIPmut} cells. Error bars represent the standard error of the proportion. N > 1800 chromosomes; results are representative for two independent experiments.

(G) Fraction of cells with micronuclei 24 h after irradiation (5Gy) in wild-type and p21^{PIPmut} cells. Error bars represent standard error of the proportion. N > 300 cells; results are representative for two independent experiments.

(H) Fraction of senescent cells three days after irradiation (5Gy) in wild-type and p21^{PIPmut} cells. Mean and standard deviation of two experiments (n > 250 cells) are shown.

(I) PCNA-mediated S phase specific degradation differentiates p21 dynamics in p53-driven DNA damage response. See also Figure S6.

- Batchelor, E., Mock, C.S., Bhan, I., Loewer, A., and Lahav, G. (2008). Recurrent initiation: a mechanism for triggering p53 pulses in response to DNA damage. *Mol. Cell* 30, 277–289.
- Batchelor, E., Loewer, A., and Lahav, G. (2009). The ups and downs of p53: understanding protein dynamics in single cells. *Nat. Rev. Cancer* 9, 371–377.
- Beckerman, R., Donner, A.J., Mattia, M., Peart, M.J., Manley, J.L., Espinosa, J.M., and Prives, C. (2009). A role for Chk1 in blocking transcriptional elongation of p21 RNA during the S-phase checkpoint. *Genes Dev.* 23, 1364–1377.
- Bunz, F. (1998). Requirement for p53 and p21 to sustain G2 arrest after DNA damage. *Science* 282, 1497–1501.
- Carpenter, A.E., Jones, T.R., Lamprecht, M.R., Clarke, C., Kang, I.H., Friman, O., Guertin, D.A., Chang, J.H., Lindquist, R.A., Moffat, J., et al. (2006). CellProfiler: image analysis software for identifying and quantifying cell phenotypes. *Genome Biol.* 7, R100.
- Cazzalini, O., Scovassi, A.I., Savio, M., Stivala, L.A., and Prosperi, E. (2010). Multiple roles of the cell cycle inhibitor p21(CDKN1A) in the DNA damage response. *Mutat. Res.* 704, 12–20.
- Chen, S.H., Forrester, W., and Lahav, G. (2016). Schedule-dependent interaction between anticancer treatments. *Science* 351, 1204–1208.
- Chung, H.K., Jacobs, C.L., Huo, Y., Yang, J., Krumm, S.A., Plemper, R.K., Tsien, R.Y., and Lin, M.Z. (2015). Tunable and reversible drug control of protein production via a self-excising degron. *Nat. Chem. Biol.* 11, 713–720.
- Ciccia, A., and Elledge, S.J. (2010). The DNA damage response: making it safe to play with knives. *Mol. Cell* 40, 179–204.
- Ciznadija, D., Zhu, X.H., and Koff, A. (2011). Hdm2- and proteasome-dependent turnover limits p21 accumulation during S phase. *Cell Cycle* 10, 2714–2723.
- Cohen, A.A., Geva-Zatorsky, N., Eden, E., Frenkel-Morgenstern, M., Issaeva, I., Sigal, A., Milo, R., Cohen-Saidon, C., Liron, Y., Kam, Z., et al. (2008). Dynamic proteomics of individual cancer cells in response to a drug. *Science* 322, 1511–1516.
- Cohen-Saidon, C., Cohen, A.A., Sigal, A., Liron, Y., and Alon, U. (2009). Dynamics and variability of ERK2 response to EGF in individual living cells. *Mol. Cell* 36, 885–893.
- Coleman, K.E., Grant, G.D., Haggerty, R.A., Brantley, K., Shibata, E., Workman, B.D., Dutta, A., Varma, D., Purvis, J.E., and Cook, J.G. (2015). Sequential replication-coupled destruction at G1/S ensures genome stability. *Genes Dev.* 29, 1734–1746.
- Debnath, J., Muthuswamy, S.K., and Brugge, J.S. (2003). Morphogenesis and oncogenesis of MCF-10A mammary epithelial acini grown in three-dimensional basement membrane cultures. *Methods* 30, 256–268.
- Deng, C., Zhang, P., Harper, J.W., Elledge, S.J., and Leder, P. (1995). Mice lacking p21CIP1/WAF1 undergo normal development, but are defective in G1 checkpoint control. *Cell* 82, 675–684.
- Doan, P., Karjalainen, A., Chandraseelan, J.G., Sandberg, O., Yli-Harja, O., Rosholm, T., Franzen, R., Candeias, N.R., and Kandhavelu, M. (2016). Synthesis and biological screening for cytotoxic activity of N-substituted indolines and morpholines. *Eur. J. Med. Chem.* 120, 296–303.
- Esashi, F., Christ, N., Gannon, J., Liu, Y., Hunt, T., Jasin, M., and West, S.C. (2005). CDK-dependent phosphorylation of BRCA2 as a regulatory mechanism for recombinational repair. *Nature* 434, 598–604.
- Finzel, A., Grybowski, A., Strasen, J., Cristiano, E., and Loewer, A. (2016). Hyperactivation of ATM upon DNA-PKcs inhibition modulates p53 dynamics and cell fate in response to DNA damage. *Mol. Biol. Cell* 27, 2360–2367.
- Galanos, P., Vougas, K., Walter, D., Polyzos, A., Maya-Mendoza, A., Haagen, E.J., Kokkalis, A., Roumelioti, F.M., Gagos, S., Tzetzis, M., et al. (2016). Chronic p53-independent p21 expression causes genomic instability by deregulating replication licensing. *Nat. Cell Biol.* 18, 777–789.
- Goolam, M., Scialdone, A., Graham, S.J.L., Macaulay, I.C., Jedrusik, A., Hupalowska, A., Voet, T., Marioni, J.C., and Zernicka-Goetz, M. (2016). Heterogeneity in Oct4 and Sox2 Targets Biases Cell Fate in 4-Cell Mouse Embryos. *Cell* 165, 61–74.
- Gottifredi, V., Shieh, S., Taya, Y., and Prives, C. (2001). p53 accumulates but is functionally impaired when DNA synthesis is blocked. *Proc. Natl. Acad. Sci. USA* 98, 1036–1041.
- Gottifredi, V., McKinney, K., Poyurovsky, M.V., and Prives, C. (2004). Decreased p21 levels are required for efficient restart of DNA synthesis after S phase block. *J. Biol. Chem.* 279, 5802–5810.
- Gut, G., Tadmor, M.D., Pe'er, D., Pelkmans, L., and Liberali, P. (2015). Trajectories of cell-cycle progression from fixed cell populations. *Nat. Methods* 12, 951–954.
- Haupt, Y., Maya, R., Kazaz, A., and Oren, M. (1997). Mdm2 promotes the rapid degradation of p53. *Nature* 387, 296–299.
- Havens, C.G., and Walter, J.C. (2009). Docking of a specialized PIP Box onto chromatin-bound PCNA creates a degron for the ubiquitin ligase CRL4Cdt2. *Mol. Cell* 35, 93–104.
- Huertas, P., Cortés-Ledesma, F., Sartori, A.A., Aguilera, A., and Jackson, S.P. (2008). CDK targets Sae2 to control DNA-end resection and homologous recombination. *Nature* 455, 689–692.
- Ira, G., Pelliccioli, A., Balijja, A., Wang, X., Florani, S., Carotenuto, W., Liberati, G., Bressan, D., Wan, L., Hollingsworth, N.M., et al. (2004). DNA end resection, homologous recombination and DNA damage checkpoint activation require CDK1. *Nature* 431, 1011–1017.
- Jin, Y., Lee, H., Zeng, S.X., Dai, M.S., and Lu, H. (2003). MDM2 promotes p21waf1/cip1 proteasomal turnover independently of ubiquitylation. *EMBO J.* 22, 6365–6377.
- Jin, Y., Zeng, S.X., Sun, X.-X., Lee, H., Blattner, C., Xiao, Z., and Lu, H. (2008). MDMX promotes proteasomal turnover of p21 at G1 and early S phases independently of, but in cooperation with, MDM2. *Mol. Cell Biol.* 28, 1218–1229.
- Kastenhuber, E.R., and Lowe, S.W. (2017). Putting p53 in Context. *Cell* 170, 1062–1078.
- Kim, Y., Starostina, N.G., and Kipreos, E.T. (2008). The CRL4 Cdt2 ubiquitin ligase targets the degradation of p21 Cip1 to control replication licensing. *Genes Dev.* 22, 2507–2519.
- Lin, J.R., Fallahi-Sichani, M., Chen, J.Y., and Sorger, P.K. (2016). Cyclic Immunofluorescence (CyclIF), A Highly Multiplexed Method for Single-cell Imaging. *Curr. Protoc. Chem. Biol.* 8, 251–264.
- Loewer, A., Batchelor, E., Gaglia, G., and Lahav, G. (2010). Basal dynamics of p53 reveal transcriptionally attenuated pulses in cycling cells. *Cell* 142, 89–100.
- Mali, P., Yang, L., Esvelt, K.M., Aach, J., Guell, M., DiCarlo, J.E., Norville, J.E., and Church, G.M. (2013). RNA-guided human genome engineering via Cas9. *Science* 339, 823–826.
- Mansilla, S.F., Soria, G., Valleria, M.B., Habif, M., Martínez-López, W., Prives, C., and Gottifredi, V. (2013). UV-triggered p21 degradation facilitates damaged-DNA replication and preserves genomic stability. *Nucleic Acids Res.* 41, 6942–6951.
- Mattia, M., Gottifredi, V., McKinney, K., and Prives, C. (2007). p53-Dependent p21 mRNA elongation is impaired when DNA replication is stalled. *Mol. Cell Biol.* 27, 1309–1320.
- Mönke, G., Cristiano, E., Finzel, A., Friedrich, D., Herzel, H., Falcke, M., and Loewer, A. (2017). Excitability in the p53 network mediates robust signaling with tunable activation thresholds in single cells. *Sci. Rep.* 7, 46571.
- Mueller, F., Senecal, A., Tantale, K., Marie-Nelly, H., Ly, N., Collin, O., Basyuk, E., Bertrand, E., Darzacq, X., and Zimmer, C. (2013). FISH-quant: automatic counting of transcripts in 3D FISH images. *Nat. Methods* 10, 277–278.
- Muñoz-Espín, D., and Serrano, M. (2014). Cellular senescence: from physiology to pathology. *Nat. Rev. Mol. Cell Biol.* 15, 482–496.
- Ng, C.C., Arakawa, H., Fukuda, S., Kondoh, H., and Nakamura, Y. (2003). p53RFP, a p53-inducible RING-finger protein, regulates the stability of p21WAF1. *Oncogene* 22, 4449–4458.
- Oliphant, T.E. (2007). Python for scientific computing. *Comput. Sci. Eng.* 9, 10–20.

- Paek, A.L., Liu, J.C., Loewer, A., Forrester, W.C., and Lahav, G. (2016). Cell-to-Cell Variation in p53 Dynamics Leads to Fractional Killing. *Cell* 165, 631–642.
- Paparrizos, J., and Gravano, L. (2015). k-Shape: Efficient and Accurate Clustering of Time Series. In Proceedings of the 2015 ACM SIGMOD International Conference on Management of Data, pp. 1855–1870.
- Purvis, J.E., Karhohs, K.W., Mock, C., Batchelor, E., Loewer, A., and Lahav, G. (2012). P53 dynamics control cell fate. *Science* 336, 1440–1444.
- Rago, C., Vogelstein, B., and Bunz, F. (2007). Genetic knockouts and knockins in human somatic cells. *Nat. Protoc.* 2, 2734–2746.
- Ran, F.A., Hsu, P.D., Lin, C.Y., Gootenberg, J.S., Konermann, S., Trevino, A.E., Scott, D.A., Inoue, A., Matoba, S., Zhang, Y., and Zhang, F. (2013). Double nicking by RNA-guided CRISPR Cas9 for enhanced genome editing specificity. *Cell* 154, 1380–1389.
- Riley, T., Sontag, E., Chen, P., and Levine, A. (2008). Transcriptional control of human p53-regulated genes. *Nat. Rev. Mol. Cell Biol.* 9, 402–412.
- Schindelin, J., Arganda-Carreras, I., Frise, E., Kaynig, V., Longair, M., Pietzsch, T., Preibisch, S., Rueden, C., Saalfeld, S., Schmid, B., et al. (2012). Fiji: an open-source platform for biological-image analysis. *Nat. Methods* 9, 676–682.
- Snijder, B., and Pelkmans, L. (2011). Origins of regulated cell-to-cell variability. *Nat. Rev. Mol. Cell Biol.* 12, 119–125.
- Starostina, N.G., and Kipreos, E.T. (2012). Multiple degradation pathways regulate versatile CIP/KIP CDK inhibitors. *Trends Cell Biol.* 22, 33–41.
- Stewart-Ornstein, J., and Lahav, G. (2016). Dynamics of CDKN1A in Single Cells Defined by an Endogenous Fluorescent Tagging Toolkit. *Cell Rep.* 14, 1800–1811.
- Strasen, J., Sarma, U., Jentsch, M., Bohn, S., Sheng, C., Horbelt, D., Knaus, P., Legewie, S., and Loewer, A. (2018). Cell-specific responses to the cytokine TGF β are determined by variability in protein levels. *Mol. Syst. Biol.* 14, e7733.
- Toettcher, J.E., Loewer, A., Ostheimer, G.J., Yaffe, M.B., and Tidor, B. (2009). Distinct mechanisms act in concert to mediate cell cycle arrest. *Proc. Natl. Acad. Sci. U. S. A.* 106, 785–790.
- Weinberger, L.S., Burnett, J.C., Toettcher, J.E., Arkin, A.P., and Schaffer, D.V. (2005). Stochastic gene expression in a lentiviral positive-feedback loop: HIV-1 Tat fluctuations drive phenotypic diversity. *Cell* 122, 169–182.

STAR★METHODS

KEY RESOURCES TABLE

REAGENT or RESOURCE	SOURCE	IDENTIFIER
Antibodies		
p53 antibody (DO-1), mouse	Santa Cruz	Cat#sc-126; RRID: AB_628082
p21 ^{WAF1} antibody (Ab-1), mouse	Calbiochem	Cat#OP64; RRID: AB_213423
p21 ^{WAF1/Cip1} antibody (12D1), rabbit	Cell Signaling Technology	Cat#2947; RRID: AB_823586
BrdU antibody, rabbit	Rockland	Cat#600-401-C29; RRID: AB_10893609
Monoclonal CyclinB1 antibody (GNS1), mouse	Thermo Fisher	Cat#MA5-14319; RRID: AB_10987286
GAPDH antibody, rabbit	Sigma-Aldrich	Cat#G9545; RRID: AB_796208
Recombinant DNA		
hCas9	(Mali et al., 2013); Addgene	Addgene#41815
hCas9n	(Mali et al., 2013); Addgene	Addgene#41816
sgRNA cloning vector	(Mali et al., 2013); Addgene	Addgene#41824
pCS6-YFP-SMASH	(Chung et al., 2015); Addgene	Addgene#68853
sgRNA_AL	This paper	N/A
sgRNA_p53-T5 (guide sequence: GGAGAATGTCAG TCTGAGTC)	This paper	N/A
sgRNA_p53-T8 (guide sequence: TCCCCTGCCATT TTGGGTTT)	This paper	N/A
sgRNA_p53-T14 (guide sequence: TCTCCCTCCCC TGCCATTTT)	This paper	N/A
sgRNA_cbx5-T2 (guide sequence: TCTTTGTTTT CGCATCCTC)	This paper	N/A
sgRNA_cbx5-T4 (guide sequence: AACAGCAAA GAGCTAAAGG)	This paper	N/A
sgRNA_cbx5-T5 (guide sequence: ACAGCAAAGA GCTAAAGGAG)	This paper	N/A
sgRNA_p21-T2 (guide sequence: GGAAGCCCTAA TCCGCCAC)	This paper	N/A
sgRNA_p21-T3 (guide sequence: GGCTTCCTGTG GGCGGATTA)	This paper	N/A
sgRNA_p21-T7 (guide sequence: CTGCAGTCCTG GAAGCGCGA)	This paper	N/A
sgRNA_p21Exon2-T2 (guide sequence: CGGCGCA GACCAGCATGAC)	This paper	N/A
sgRNA_p21Exon2-T3 (guide sequence: GCATGTCCG CACCTGTCATGC)	This paper	N/A
pC2aN	This paper	N/A
pAAV-CBX5-CeSEPT	This paper	N/A
pAAV-p53-VSEPT	This paper	N/A
pAAV-p21-CSEPT	This paper	N/A
pDO-p21 ^{mut} -mCherry-smash-p2a-neo	This paper	N/A
pDO-p21-P2A-mCherry-BSD	This paper	N/A
Chemicals, Peptides, and Recombinant Proteins		
5-Bromo-2'-deoxyuridine (BrdU)	Sigma-Aldrich	Cas#59-14-3
Asunaprevir (ASV)	American Radiolabeled Chemicals, Inc	Cas#630420-16-5
Anti-Evaporation Oil	Ibidi	Cat#50051
Rat Tail Collagen I	Corning	Cat#354236

(Continued on next page)

Continued

REAGENT or RESOURCE	SOURCE	IDENTIFIER
Hoechst 33342	Invitrogen	Cat#H3570
Propidium Iodide	Acros Organics	Cas#25535-16-4
RNase A	AppliChem	Cat#9001-99-4
DNase I	Roche	Cat#4716728001
FluoroBrite	Thermo Fisher	Cat#A1896701
HEPES	Thermo Fisher	Cat#A15630106
G418	Biochrom	Cat#A2912
Lipofectamine 3000 Transfection Reagent	Thermo Fisher	Cat#L3000015
RO3306	Axon Medchem	Cat# 1530
Neocarcinostatin (NCS)	Sigma-Aldrich	Cas#9014-02-2
Critical Commercial Assays		
Phire Animal Tissue Direct PCR Kit	Thermo Fisher	Cat#F140WH
T7 Endonuclease I	New England BioLabs	Cat#M0302S
QIAquick Gel Extraction Kit	QIAGEN	Cat#28706
QIAprep Spin Miniprep Kit	QIAGEN	Cat#27106
QIAquick DNA Mini Kit	QIAGEN	Cat#51306
EdU Click-647	Carl Roth	Cat#7777.1
Gibson Assembly® Master Mix	New England BioLabs	Cat#E2611L
Deposited Data		
Single cell time series	This paper	https://doi.org/10.17632/zsd79s262s.1
Experimental Models: Cell Lines		
Human: HEK293T	ATCC	CRL-3216
Human: MCF10A	ATCC	CRL-10317
Human: A549	ATCC	CRM-CCL-185
Human: MCF7	ATCC	HTB-22
Human: RPE1-hTERT	ATCC	CRL-4000
Human: MCF10A p53 ^{Y/+} / cbx5 ^{C/C}	This paper	N/A
Human: MCF10A p53 ^{Y/R} / cbx5 ^{C/C}	This paper	N/A
Human: MCF10A p21 ^{R/+} / p53 ^{Y/+} / cbx5 ^{C/C} (also indicated as p21 ^{wt} in Figure 4)	This paper	N/A
Human: MCF10A p21 ^{PIPmut}	This paper	N/A
Human: MCF10A p21 ^{2a-R/+} / p53 ^{Y/+} / cbx5 ^{C/C} (transcriptional reporter)	This paper	N/A
Oligonucleotides		
see Table S1	This paper	N/A
Bacterial and Virus Strains		
Ad-cre virus stock	Vector Biolabs	Cat #1045
Software and Algorithms		
Custom image analysis algorithms	This paper	N/A
FlowJo software	FlowJo, LLC	https://www.flowjo.com/
Fiji	Schindelin et al., 2012	https://imagej.net/Fiji
MATLAB	MathWorks	https://www.mathworks.com/
Mathematica	Wolfram	https://www.wolfram.com/mathematica/
Python	https://www.python.org/	N/A
NIS-Elements Advanced Research	Nikon	https://www.nikoninstruments.com/en_DE/Products/Software/NIS-Elements-Advanced-Research

(Continued on next page)

Continued

REAGENT or RESOURCE	SOURCE	IDENTIFIER
Other		
Inverted fluorescence microscope	Nikon	Ti-E inverted
Biological irradiator	Precision X-Ray	X-RAD 320
Glass bottom microwell dishes	MatTek	Part No: P35G-1.5-14-C
μ -Plate 24 Well Black	ibidi	Cat#82406
μ -Dish 35 mm, high	ibidi	Cat# 81156

CONTACT FOR REAGENTS AND RESOURCE SHARING

Further information and requests for resources and reagents should be directed to and will be fulfilled by the Lead Contact, Alexander Loewer (loewer@bio.tu-darmstadt.de).

EXPERIMENTAL MODEL AND SUBJECT DETAILS**Cell lines**

The female human non-transformed breast epithelial cell line MCF10A was maintained in Dulbecco's Modified Eagle Medium supplemented with 5% horse serum, 20 ng/ml EGF, 0.5 μ g/ml Hydrocortisone, 100 μ g/ml Cholera toxin and 10 μ g/ml Insulin according to established protocols (Debnath et al., 2003). The female human adenocarcinoma cell line MCF7 derived from breast epithelial tissue was maintained in RPMI 1640 with 10% fetal calf serum; the male human carcinoma cell line A549 derived from lung epithelial tissue and the female human osteosarcoma cell line U-2 OS derived from a sarcoma of the tibia, were maintained in McCoy's 5A with 10% fetal calf serum. All media contained 2mM Glutamax, 100 U/ml penicillin and 100 μ g/ml streptomycin. All cell lines were cultured at 37°C with 5% CO₂ at saturated humidity.

METHOD DETAILS**Plasmids and cloning**

Cas9 (Addgene plasmid # 41815), Cas9n (Addgene plasmid # 41816) and sgRNA cloning vector (Addgene plasmid # 41824) are gifts from George Church's lab (Mali et al., 2013). We modified the sgRNA cloning vector by inserting about 80 base pairs and an AgeI site (the final product named sgRNA_AL) to reduce the cost and complexity for cloning further sgRNAs. All guide sequences were selected using CRISPR Design tool (<http://crispr.mit.edu>). Efficiency of sgRNAs was tested using T7 endonuclease I assay in HEK293T cells (Ran et al., 2013). Repair templates were generated using Gibson Assembly (New England Biolabs). The SMASH fragment was amplified from pCS6-YFP-SMASH, a gift from Michael Lin (Addgene plasmid # 68853). All primer sequences are listed in supplemental Table S1, vector maps and sequences are available upon request.

Cell line engineering

To tag endogenous loci, MCF10A cells were seeded in a 12-well plate at a density of 2.5×10^5 cells/well 24 hours prior to transfection and transfected with 495 ng Cas9n or Cas9 plasmid, 495 ng sgRNA plasmids and 10 ng linearized repair template DNA using Lipofectamine 3000 according to manufacturer's recommendations. After 3 days, cells were transferred to 10 cm plates and selected with G418 (400 μ g/ml). For generating p21^{PIPmut} cell line, 1 μ M asunaprevir (ASV) was added in the medium from the time of transfection to degrade stabilized mutant p21. After about 2 weeks, single-cell derived colonies were screened by PCRs using Phire Animal Tissue Direct PCR Kit. Untagged alleles from heterozygotes were sequenced to ensure that no alterations occurred. Four most-likely off-target regions were amplified and sequenced. Excision of selection cassettes was performed as previously described (Rago et al., 2007). In brief, 5×10^5 cells of selected clones were plated in a 25 cm² cell culture flask. 24 hours later, 1 mL of Ad-cre virus stock (10^7 plaque forming units) was added to the flask and incubated for 24 hours. Then cells were rinsed with 1x HBSS, detached with 1 mL of trypsin-EDTA, diluted to 50~100 cells/10 mL and seeded in 10 cm plates. After another two weeks, each colony was moved into two separate wells for negative selection. G418-sensitive lines were carefully validated by cell cycle assay, microscopy and western blot.

Time-lapse microscopy

1.5×10^5 cells were plated in 35 mm collagen-coated glass bottom dishes (MatTek), 35 mm μ -dishes or 24-well μ -plates (both ibidi) two days before experiments. If applicable, 10 μ M R03306 was added 16 h before the experiment for synchronization in G2-phase. Two hours before imaging, cells were washed twice with 1xPBS and incubated in FluoroBrite supplemented with 0.5% horse serum and growth factors (see above). If necessary, 1 mL Anti-Evaporation Oil (ibidi) was added on the top of medium to prevent evaporation. Dishes were placed in an incubation chamber with constant temperature (37°C), CO₂ concentration (5%), and humidity. Cells

were imaged every 15 min or 20 min on a Nikon Ti inverted fluorescence microscope with a Hamamatsu Orca R2 or Nikon DS-Qi2 camera and a 20x plan apo objective (NA 0.75) controlled by Nikon Elements software. Appropriate filter sets were used (mCerulean: 438/24 nm excitation (EX), 458 nm dichroic beam splitter (BS), 483/32 nm emission (EM); mVenus: 500/24 nm EX, 520 nm BS, 542/27 nm EM; mCherry: 562/40 nm EX, 593 nm BS, 624/40 nm EM; Cy5: 628/40 nm EX, 692/40 nm EM; DAPI: 387/11 nm EX, 409 nm BS, 447/60 nm EM). Double strand DNA breaks were induced by X-ray irradiation at dose rate of 1Gy / 26 s (250 KeV, 10 mA).

Image analysis

As previously described (Finzel et al., 2016), cells were isolated and tracked from time-series images using custom-written MATLAB scripts based on codes developed by the Alon lab (Cohen et al., 2008) and the CellProfiler project (Doan et al., 2016). In brief, we first applied flat field correction and background subtraction to raw images. Then image registration was performed with a custom Python3-based tool to compensate for movement from removing dishes for irradiation and/or endpoint assays. In brief, shifted pixels between two images were identified from the maximum convolution calculated using fast Fourier transform method (scipy package (Oliphant, 2007)). The biggest common area was then cropped for all time points. We next segmented individual nuclei from nuclear marker images using thresholding and seeded watershed algorithms. Segmented cells were then tracked in time series images using a greedy match algorithm. Only cells trackable through the full period of experiments were considered. Cells were tracked in backward direction from the last to the first-time point.

Single cell clustering

Similarity between trajectories was calculated using shape-based distance (SBD) as previously defined (Paparrizos and Gravano, 2015). In brief, p21 signals after irradiation were Z-normalized to remove scaling variance. The distance between each two pair of trajectories was defined based on cross-correlation, which is able to remove shift variances. This resulted in a vector for each cell, representing the similarity between it and all other cells (including itself). Based on these vectors, K-centroids clustering ($k = 2$) and binary tree were performed and resulted in four subpopulations of trajectories with different shapes. All the scripts for SBD-based clustering were written in MATLAB.

Feature analysis of single cell trajectories

The feature analysis of single cell trajectories was performed using self-written MATLAB scripts. As shown in Figure S2C, the steady-state level measured during non-stressed periods was determined as basal level (e.g., C_0^{p53} indicates basal level of p53). Once the protein level increased to as much as 1.3x the basal level, a 'pulse' was considered to form; once it went down to basal level and accumulated again to 1.3x the basal level, second 'pulse' was considered to form and so on. This filter, which applies to both p53 and p21, allowed capturing the main patterns while removing noise (e.g., T_{1st}^{p21} and T_{1st}^{p53} indicate first peak time of p21 and p53). In some cells, the sustained p21 may be too weak ($< 1.3x$) to be counted as a 'pulse'. To determine the time when cells start to respond, we defined reacting time as the time when protein levels reach the 15 percentiles of the difference between peak and basal levels (T_{rct}^{p53}). To determine how fast dynamics moved down, we defined the failing rate — the averaged rate dynamics moved from peak down to basal level (if not, endpoint level).

Cell cycle progression

To assess the initial cell cycle phases during live-cell imaging, cell division events were monitored and analyzed for a duration of 20~24 hours prior to irradiation, followed by DNA damage induction and imaging for additional 24 hours. The time of cell division was used to estimate cell cycle phase at time of damage. Individual labeling experiments were performed to validate this estimation (see Figure 2B for details). Final cell cycle measurement was performed as previously described (Gut et al., 2015). Briefly, 10 μ M EdU (EdU Click-647, Carl Roth GmbH + Co. KG) was added to cell cultures 30 minutes before the end of live-cell imaging and detected immediately after imaging. EdU intensities were sorted and an edge detection algorithm was performed to identify S phase cells. In order to distinguish G1 and G2 phase cells, Hoechst staining was performed to measure the DNA content and nuclear sizes, upon which cells were classified into two groups (G1-phase and G2-phase) using unsupervised classification.

Considering that mutant p21 may alter normal cell cycle progression in p21^{PIPmut} cells, we performed double-pulse labeling experiment instead. Briefly, p21^{PIPmut} cells were incubated in 10 μ M of BrdU and EdU for 30 min before and 24 hours after irradiation, respectively. After live-cell imaging, cells were fixed with 2% paraformaldehyde, permeabilized with 0.1% Triton X-100 in 1xPBS and blocked with 10% goat serum in 1xPBS. Then endogenous fluorescent fusion proteins were bleached with 3% H₂O₂ and 20 mM HCL (Lin et al., 2016) in order to free fluorescent channels for subsequent immunofluorescence staining. EdU detection was performed following manufacturer's instruction (EdU Click-647, Carl Roth GmbH + Co. KG). Then primary antibody against BrdU (1:500, anti-rabbit, Rockland) in DNaseI (0.01 unit/ μ l) and secondary antibody (Alexa Fluor 488, 1:700, anti-rabbit) were used to detect BrdU, followed by Hoechst staining and imaging. Before automated cell segmentation and tracking, endpoint images were aligned to live-cell images by an image registration tool written in Python3.

Flow cytometry-based cell cycle analysis

To validate endogenous reporters, wild-type MCF10A, p53^{Y/+} / cbx5^{C/C} cells and p21^{R/+} / p53^{Y/+} / cbx5^{C/C} cells were plated at a density of 3~3.5x10⁵ cells in 6 cm plates two days before experiments. Cells were exposed to 5Gy X-ray radiation, harvested at indicated time points, washed with 1xPBS, fixed with ice-cold 80% Ethanol / 20% 1xPBS and stored at -20°C until all samples were collected. During flow cytometry analysis, cells were washed with 1xPBS and stained with 25 µg/ml PI in 0.1% Triton 1xPBS with 0.2 mg/ml RNase A and analyzed using flow cytometry (Cytomics FC500, Beckman Coulter). Cell cycle phases were determined based on the DNA content in FlowJo software (FlowJo, LLC).

Single-cell Immunofluorescence

Cells were plated at a density of 1.5x10⁵ cells in 3.5 cm collagen-coated glass bottom dishes (MatTek) or at a density of 2x10⁵ cells on coated poly-L-lysine coverslips in 6 well plates two days before experiments. After irradiation, cells were fixed at indicated time points with 2% paraformaldehyde. Cells were permeabilized with 0.1% Triton X-100 in 1xPBS, blocked with 10% goat serum in 1xPBS, incubated with primary antibody in 1% BSA in 1xPBS, washed with 0.1% Triton X-100 in PBS, and incubated with secondary antibody conjugated with Alexa Fluor 488 / 647 (Thermo Fisher Scientific) in 1% BSA in PBS. After washing, cells were counterstained with 2 µg/ml Hoechst in 0.1% Triton X-100/PBS and imaged with a 20x plan apo objective (NA 0.75) using appropriate filter sets. Automated segmentation was performed in MATLAB (MathWorks) with algorithms from CellProfiler (Carpenter et al., 2006). Manual counting was performed blinded.

smFISH hybridization

MCF10A cells were cultured for 24 h on 18 mm uncoated coverglass (thickness #1). Cells were washed on ice, fixed with 2% Paraformaldehyde for 10 min at room temperature and permeabilized over night with 70% Ethanol at 4°C. Custom probe sets for single molecule FISH labeled with CalFluor-610, were designed using Stellaris RNA FISH probe designer (Biosearch Technologies) on the reference sequences NM_000389.4. Hybridization was performed at a final concentration of 0.1 µM probe following manufacturer's instructions. Following hybridization procedure, cells were stained with EdU Click-488 ROTI kit for imaging (Carl Roth) for 15 min according to manufacturer's instructions. Cover glasses were mounted on Prolong Gold Antifade (Molecular probes, Life technologies). For single molecule RNA quantification, 21 z stacks of each cell were acquired with 300 nm step-width. Quantification of RNA counts per cell was performed using FISH Quant (Mueller et al., 2013) and custom written MATLAB software. About 50 cells were analyzed.

Immunoblotting

Cells were plated at a density of 3.5x10⁵ cells in 6 cm plates two days before experiments. After irradiation, cells were harvested at indicated time points to extract proteins by lysis in the presence of protease and phosphatase inhibitors. BCA assay (Thermo Fisher Scientific) was used to measure total protein concentrations. Equal amounts of protein were separated by electrophoreses on 10% SDS polyacrylamide gels and transferred to nitrocellulose membranes (Thermo Fisher Scientific) by electroblotting (Bio Rad). We blocked membranes with 5% non-fat dried milk, incubated them overnight with primary antibody, washed them, incubated them with secondary antibody coupled to peroxidase (#31460, Thermo Fisher Scientific), washed again and detected protein levels using chemoluminescence (ECL Prime, GE Healthcare).

Metaphase chromosome analysis

Cells were plated at a density of 5x10⁵ cells in 10 cm plates two days before experiments. 30 min before irradiation, 10 µM EdU (Carl Roth) was added. After incubation, EdU was removed, cells were washed and irradiated with 5Gy X-rays. 22 h after irradiation, we added 100 µg/ml Colcemid (GIBCO) and 5 mM Caffeine and harvested cells 2 h later. Cells were pelleted by centrifugation, resuspend in 75mM KCl and incubated for 35 min at 37°C. After centrifugation, 10 mL fresh fixative (3 parts Methanol, 1 part 100% acetic acid) was added dropwise while vortexing. After 10 min incubation, this step was repeated twice with intervening incubations at 4°C. Chromosomes were spread by dropping resuspended cells to a coverslip. EdU staining was performed following manufacturer's instructions (EdU Click-647, Carl Roth), DNA was stained with 2µg/ml Hoechst 33342 in 0.1% Triton/PBS. After final wash steps in PBS, coverslips were mounted in Prolong Antifade.

Senescence-associated β-Galactosidase assay

0.3 × 10⁵ cells were seeded 2 days before being irradiated with 5Gy. 3 days after irradiation, cells were fixed with 2% paraformaldehyde/0.2% glutaraldehyde (Sigma-Aldrich), washed in 1x PBS and incubated for 20 h in staining solution (150 mM NaCl, 40 mM citric acid, 40 mM NaH₂PO₄, 2 mM MgCl₂, 5 mM K₄Fe(CN)₆, 5 mM K₃Fe(CN)₆, and 1 mg/ml X-gal, all Carl Roth). Stained cells were manually quantified.

Mathematical modeling

The model was implemented in Wolfram Mathematica 11 by different delay differential equations (DDEs) depending on the cell cycle characteristics of the considered cell, i.e., its initial cell cycle phase and its cell cycle stage at the end of the measurement.

For cells that were irradiated in the G1 phase and progressed to S phase, the p21 dynamics was modeled by the following DDEs:

$$\frac{d[p21(t)]}{dt} = \begin{cases} \frac{m \cdot [p53(t - \tau)]^n}{\theta^n + [p53(t - \tau)]^n} - \delta \cdot [p21(t)], & t < t_S \\ - \delta \cdot [p21(t)], & t \geq t_S \end{cases} \quad (\text{Model 1.1})$$

$$\frac{d[p21(t)]}{dt} = \begin{cases} \frac{m \cdot [p53(t - \tau)]^n}{\theta^n + [p53(t - \tau)]^n} - \delta \cdot [p21(t)], & t < t_S \\ \frac{m \cdot [p53(t - \tau)]^n}{\theta^n + [p53(t - \tau)]^n} - \delta \cdot D_S \cdot [p21(t)], & t \geq t_S \end{cases} \quad (\text{Model 2.1})$$

where t_S indicates the onset of S phase.

In model 2, p21 degradation is suddenly increased by the factor D_S after the beginning of S-phase. However, as CRL4^{Ctd2} substrates are degraded in sequential order with p21 being a less affine substrate (Coleman et al., 2015), it is reasonable to assume a gradual increase of the degradation rate upon S-phase entry, which we implemented in the following model:

$$\frac{d[p21(t)]}{dt} = \begin{cases} \frac{m \cdot [p53(t - \tau)]^n}{\theta^n + [p53(t - \tau)]^n} - \delta \cdot [p21(t)], & t < t_S \\ \frac{m \cdot [p53(t - \tau)]^n}{\theta^n + [p53(t - \tau)]^n} - \delta \cdot D_S(t) \cdot [p21(t)], & t \geq t_S \end{cases} \quad (\text{Model 3.1})$$

with

$$D_S(t) = 50 - 49 \cdot \exp(-0.25 \cdot t + 0.25 \cdot t_S).$$

As we lacked quantitative information about the biological processes underlying such a gradual increase of the degradation rate, we chose a simple saturation function for $D_S(t)$ that preserves continuity at the onset of S phase, i.e., $D_S(t_S) = 1$, and reaches a maximum value of $D_{S,\infty} = 50$, corresponding to the value of D_S in model 2. An illustration of this function is shown in Figure S5J.

Mathematica 11 was also used to fit the model to the p21 data of single cells. Before performing the fits, the background, which was estimated by the smallest measured value, was subtracted from the p21 and p53 data of each cell. We performed the fits using the 'NonlinearModelFit' function with the 'NMinimize' method. For the minimization of the quantity $\chi^2 = \sum |r_i|^2$, where the r_i are residuals giving the difference between each original data point and its fitted value, the Nelder-Mead algorithm ('NelderMead') was used. We set the maximum number of iterations ('MaxIterations') to 2000 and the 'AccuracyGoal' as well as the 'PrecisionGoal' to 50. The constraints and the start values that were used to fit the model parameters are shown in Table 1 (see Table S2 for further details):

For cells that were irradiated in S-phase and progressed to G2, we set the value of the degradation rate to $\delta = 0.2$ and did not fit it, as otherwise the fitting procedure took very long and the algorithm tended to find solutions with $\delta \approx 0$, which would not be realistic. Furthermore, for model 2, we assumed that the degradation rate was $D_S = 50$ times higher during S phase than in G1 or G2, unless indicated otherwise. The time delay τ was always set to $\tau = 1.4$ h, since we presumed that the delay in p21 expression due to the duration of transcription and translation should be similar for every cell. In addition, we chose a hill coefficient of $n = 4$ for the p53-dependent p21 activation, as p53 is a tetramer. In order to ensure a good fit quality and to make sure that our results did not depend on the provided initial values for the fit parameters, we performed for each considered cell a fit with 20 different randomly chosen initial values of the fit parameters and selected the best fit for averaging, unless indicated otherwise.

The following parameters were used for the presented single cell fits: $m = 218.66$, $\theta = 209.84$, $\delta = 0.27$ (Figure 3B); $m = 82.83$, $\theta = 232.46$, $\delta = 0.16$ (Figure 3C); $m = 399.73$, $\theta = 204.90$, $\delta = 0.77$, $D_S = 50$, $t_S = 9.32$ (Figure 3D); $m = 28.08$, $\theta = 152.11$, $\delta = 0.2$, $D_S = 50$, $t_S = 12.84$ (Figure 3E). $m = 418.65$, $\theta = 196.18$, $\delta = 0.85$, $t_S = 8.33$ / $m = 27.88$, $\theta = 151.02$, $\delta = 0.2$, $t_S = 12.74$ (Figure S5F, G1-S / S-G2); $m = 398.31$, $\theta = 204.76$, $\delta = 0.77$, $t_S = 8.92$ (Figure S5I, model gradually incr. deg.).

For p21^{PIPmut} cells, we assumed unaltered p21 degradation and transcription rates during S phase and hence modeled the p21 dynamics for all cell cycle phases by

$$\frac{d[p21(t)]}{dt} = \frac{m \cdot [p53(t - \tau)]^4}{\theta^4 + [p53(t - \tau)]^4} - \delta \cdot [p21(t)]. \quad (\text{Model 4})$$

In this case, we fitted the p21 dynamics only for the first 10 hours after the irradiation and assumed a slightly smaller time delay of $\tau = 1.2$ h. Apart from that, the fits were performed in the same way as described in the previous paragraph (see Table S3 for further details).

QUANTIFICATION AND STATISTICAL ANALYSIS

Quantitative analysis of single cell data was performed in MATLAB (Mathworks) and Mathematica 11 (Wolfram). Details can be found in each figure legend.

DATA AND SOFTWARE AVAILABILITY

Our custom analysis code is available from the lead contact upon reasonable request. Single cell trajectories are available for download from Mendeley Data (<https://doi.org/10.17632/zsd79s262s.1>).